




# Large mobility modulation in ultrathin amorphous titanium oxide transistors

Nikhil Tiwale <sup>1</sup>, Ashwanth Subramanian<sup>2</sup>, Zhongwei Dai<sup>1</sup>, Sayantani Sikder<sup>2</sup>, Jerzy T. Sadowski <sup>1</sup> & Chang-Yong Nam <sup>1,2</sup>✉

Recently, ultrathin metal-oxide thin film transistors (TFTs) have shown very high on-off ratio and ultra-sharp subthreshold swing, making them promising candidates for applications beyond conventional large-area electronics. While the on-off operation in typical TFTs results primarily from the modulation of charge carrier density by gate voltage, the high on-off ratio in ultrathin oxide TFTs can be associated with a large carrier mobility modulation, whose origin remains unknown. We investigate 3.5 nm-thick TiO<sub>x</sub>-based ultrathin TFTs exhibiting on-off ratio of  $\sim 10^6$ , predominantly driven by  $\sim 6$ -decade gate-induced mobility modulation. The power law behavior of the mobility features two regimes, with a very high exponent at low gate voltages, unprecedented for oxide TFTs. We find that this phenomenon is well explained by the presence of high-density tail states near the conduction band edge, which supports carrier transport via variable range hopping. The observed two-exponent regimes reflect the bi-exponential distribution of the density of band-tail states. This improved understanding would be significant in fabricating high-performance ultrathin oxide devices.

<sup>1</sup>Center for Functional Nanomaterials, Brookhaven National Laboratory, Upton, NY 11973, USA. <sup>2</sup>Department of Materials Science and Chemical Engineering, Stony Brook University, Stony Brook, NY 11794, USA. ✉email: [cynam@bnl.gov](mailto:cynam@bnl.gov)

Thin film transistors (TFTs) made of semiconducting metal oxide have been extensively investigated over the past decades, primarily as a higher-mobility, low-cost alternative to conventional amorphous Si in large area electronics applications such as active matrix displays<sup>1–3</sup>. On the other end of the spectrum, in the domain of high-performance computing, the single-crystalline Si-based technology is approaching its physical limits, and atomically thin two-dimensional material systems have been garnering extensive interests in pursuit of gaining ultimate electronic control on the transistor channel. As a matter of fact, fully depleted Si-on-insulator (FD-SOI) technology, using ultrathin Si layer has shown profound impacts on low-power computing devices<sup>4</sup>. To this end, complex oxide materials have also been used to fabricate TFTs based on two-dimensional electron gas (2DEG), where the carrier transport is highly confined near the insulator-semiconductor interface<sup>5</sup>. Primarily, such reports have been focused on epitaxially grown oxides, limiting their scalability in practical applications. However, the 2DEG formation has been reported recently in a rather simple TiO<sub>2</sub>/Al<sub>2</sub>O<sub>3</sub> interface fabricated by atomic layer deposition (ALD)<sup>6,7</sup>, showing promises for scaling up this device architecture for more practical applications. In addition, sputter-deposited 1-nm-thick indium tin oxide transistors have shown to reach near-ideal subthreshold swing and nearly no drain-induced barrier lowering<sup>8</sup>. These recent reports clearly indicate growing interests in ultrathin oxide TFTs.

An interesting observation among the ultrathin channel devices and 2DEG transistors is that they typically exhibit sharp and very high on-off ratios in the transfer characteristics with extremely low off currents; the channel is essentially fully depleted of charge carriers in the off-state, and the gate induced charge accumulation leads to many decades of increases in the drain current, driving the transistor into on-state. In general, the working of conventional TFTs exhibit many orders of gate-dependent charge carrier density modulation, while the extent of gate-induced mobility modulation has been limited to only a few decades<sup>9–12</sup> or has not been studied in detail<sup>13–15</sup>. A large gate-dependent mobility modulation is uncommon in conventional amorphous Si TFT devices, and a clear picture elucidating the origin of mobility modulation in ultrathin metal oxide TFTs has not been reported so far<sup>11,16</sup>. Since the on-off current modulation in TFTs is essentially from the combined effect of both carrier density and mobility modulations, it is worth examining if such mobility modulation is a universal phenomenon in amorphous-oxide TFTs. Moreover, it may have general implications on further improving the performance of the ultrathin oxide devices.

TiO<sub>2</sub> as a semiconductor is extensively used in solar cells<sup>17–20</sup> and photocatalysis<sup>21–24</sup>, but its application as a TFT channel material has not been much explored. For those reported so far, TiO<sub>2</sub> layers were mostly thicker than ~10 nm and crystalline<sup>9,25–34</sup>, with only a few reporting the mobility modulation<sup>9,10</sup>. A large extent of mobility modulation, as high as ~9 decades, has been recently reported from mixed amorphous-crystalline TiO<sub>x</sub> TFT<sup>35</sup>, with its origin remaining unexplained nevertheless.

In this report, we utilize ultrathin (3.5 nm) amorphous TiO<sub>x</sub> film deposited by low-temperature ALD to fabricate TFT devices and investigate the origin of large gate-induced mobility modulation. Based on the analysis of gate-dependent mobility and control experiments involving post-ALD thermal treatments, we find that the mobility modulation is caused by the presence of high density of band-tail states that mediate the variable range hopping (VRH) of charge carriers near the mobility edge of conduction band.

## Results and discussion

**Performance of ultrathin TiO<sub>x</sub> TFT.** We fabricated bottom-gate TFTs based on the 3.5-nm-thick ultrathin amorphous TiO<sub>x</sub> thin

film deposited on Si substrates with 300 nm SiO<sub>2</sub> by low-temperature ALD at 85 °C using titanium (IV) isopropoxide and water as reactants. The deposited film was subjected to a two-step forming gas annealing at 400 °C and 600 °C (each for 15 min), and Al-based source and drain electrodes with channel length of 5 μm and width 500 μm were patterned by electron-beam lithography as shown in the schematic in Fig. 1a. The ultrathin TiO<sub>x</sub> film, after the default forming gas annealing treatment, was found to be nearly amorphous with minor nano-crystallinity, as it can be seen in the X-ray diffraction (XRD) spectra depicted in Fig. 1b. Despite using slow acquisition rate of the XRD spectra (scan rate of 0.38° min<sup>-1</sup>; total scan time of 3 h), no significant crystallinity could be observed, except for the two very weak scattering peaks likely originating from either rutile or anatase TiO<sub>x</sub><sup>17,24</sup>. Moreover, the highly surface-sensitive, low-energy electron diffraction (LEED) pattern acquired from the TiO<sub>x</sub> (inset in Fig. 1b) shows uniform, diffused background with no discernable diffraction features, further confirming the amorphous nature of prepared ultrathin TiO<sub>x</sub> film.

The transistor output characteristics measured from the fabricated ultrathin TiO<sub>x</sub> TFT shown in Fig. 2a display linear ohmic characteristics at low drain voltage ( $V_d$ ) across the entire range of gate voltages ( $V_g$ ), whereas toward the high  $V_d$  the drain current ( $I_d$ ) tends to saturate. Accordingly, the transfer characteristics measured in the saturation regime ( $V_d = 70$  V), as depicted in Fig. 2b, shows ~6 decades of on-off ratio, the subthreshold swing of 3.6 V/dec, the turn-on voltage ( $V_{on}$ ) of ~24.6 V, and the threshold voltage ( $V_{th}$ ) of ~48.5 V, with the

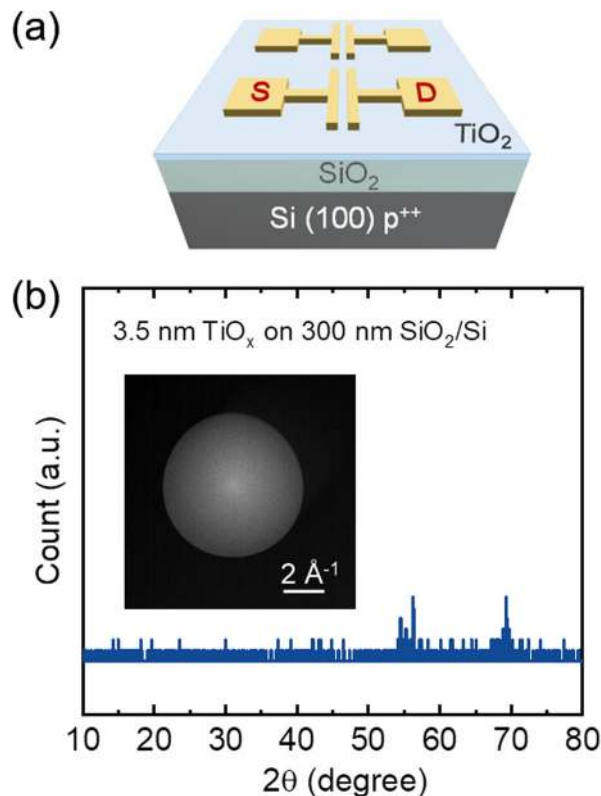


**Fig. 1** Design of the ultrathin TiO<sub>x</sub> TFT and its structural characterization.

**a** Schematic of the TiO<sub>x</sub> TFT device investigated; **b** XRD pattern acquired from 3.5-nm-thick TiO<sub>x</sub> thin film displaying no significant crystallinity except for weak scattering peaks potentially corresponding to anatase/rutile phases. The inset shows LEED image of the TiO<sub>x</sub> thin film where the lack of any discernable crystalline peaks confirms the near amorphous structure of ultrathin TiO<sub>x</sub>.

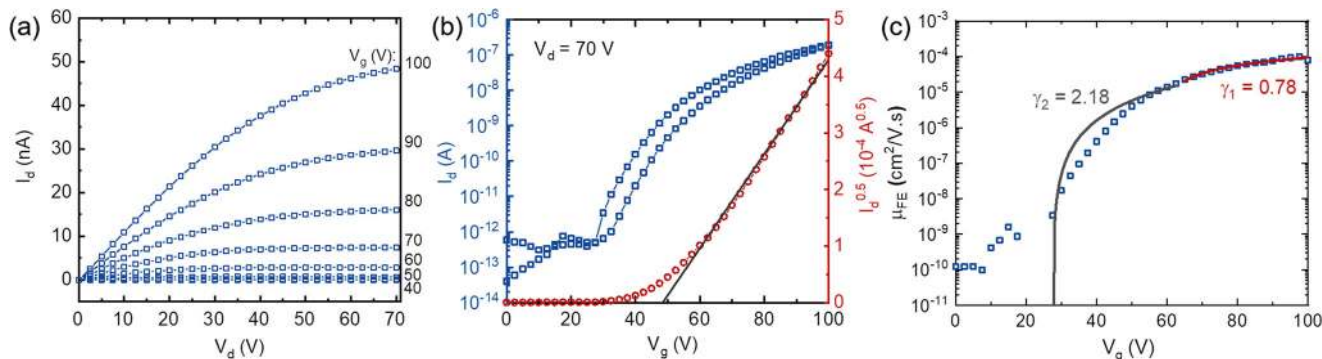


**Fig. 2 Performance of ultrathin  $\text{TiO}_x$  TFT and  $\mu_{\text{FE}}$ .** Electrical characteristics of the  $\text{TiO}_x$  TFT ( $W/L = 500 \mu\text{m}/5 \mu\text{m}$ ) fabricated using ultrathin  $\text{TiO}_x$  film annealed in forming gas (15 min at  $400^\circ\text{C}$  followed by 15 min at  $600^\circ\text{C}$ ). **a** Output characteristics depicting linear-ohmic behavior at low  $V_d$  evolving into hard saturation at high  $V_d$ ; **b** Transfer characteristics at  $V_d = 70 \text{ V}$  showing high on-off ratio ( $\sim 6$  decades),  $V_{\text{on}}$  of  $\sim -24.6 \text{ V}$ , and  $V_{\text{th}}$  of  $\sim -48.5 \text{ V}$ ; **c**  $V_g$ -dependent  $\mu_{\text{FE}}$  with power law fitting for  $V_g > 60 \text{ V}$  and  $V_g < 60 \text{ V}$ , respectively. The exponent value of 0.78 for  $V_g > 60 \text{ V}$  corresponds to the TLC, whereas the value of 2.18 for  $V_g < 60 \text{ V}$  suggests VRH transport.

relatively large difference between  $V_{\text{on}}$  and  $V_{\text{th}}$  hinting the presence of a large population of trap states<sup>36</sup>. The saturation mobility ( $\mu_{\text{sat}}$ ) of the TFT was then calculated using the standard expression,

$$\mu_{\text{sat}} = \frac{2L}{WC_i} \left( \frac{\partial \sqrt{I_d}}{\partial V_g} \right)^2, \quad (1)$$

where  $L$  represents channel length,  $W$  channel width, and  $C_i$  insulator capacitance per unit area. The  $\mu_{\text{sat}}$  in the device under the discussion was  $\sim 1.6 \times 10^{-4} \text{ cm}^2 \text{ V}^{-1} \text{ s}^{-1}$ . While the acquired mobility is lower than the crystalline  $\text{TiO}_2$  TFTs reported previously<sup>25,27,29,32</sup>, it is comparable to those reported from the TFTs fabricated using lower crystallinity  $\text{TiO}_2$ <sup>10,33,37</sup>. We further evaluated the gate dependence of field-effect mobility ( $\mu_{\text{FE}}$ ) using the general expression (Eq. (2))<sup>38,39</sup> and observed a large,  $\sim 6$ -decade gate-dependent modulation of  $\mu_{\text{FE}}$  (Fig. 2c).

$$\mu_{\text{FE}} = \frac{L}{V_d WC_i} \left( \frac{\partial I_d}{\partial V_g} \right). \quad (2)$$

Interestingly, as seen in Fig. 2c, the TFT also exhibits  $\sim 6$  decades of mobility modulation. While the magnitude of mobility modulation generally observed in  $\text{TiO}_x$  TFTs has been 2–3 decades or less<sup>9,10</sup>, modulation of  $\sim 9$  decades has also been reported for sputter-deposited 20-nm-thick  $\text{TiO}_{2-x}$  TFTs followed by vacuum annealing<sup>35</sup>.

**Power law behavior of charge mobility.** Given the  $\sim 6$  decades of on-off ratio observed in our ultrathin  $\text{TiO}_x$  TFT, the current modulation is thus predominantly originating from the gate-induced mobility modulation while the carrier density modulation by gate providing only a minor contribution. We can safely exclude possible effects of contact Schottky barrier on the observed mobility modulation considering the choice of Al electrode that has been shown to form an ohmic contact on  $\text{TiO}_x$ <sup>26,29,33,37,40</sup> and the negligible barrier height lowering effected by gate bias (Supplementary Note 1). The origin of gate-induced mobility modulation has been previously speculated to be related with the sub-bandgap trap states (localized tail states)<sup>41,42</sup>, typically present near the conduction band edge ( $E_c$ ) of amorphous semiconductors with an exponential decrease in their density of states. Particularly, Lee et al. have proposed a power law dependence of the saturation-regime  $\mu_{\text{FE}}$  on  $V_g$  with

the following expression<sup>16,42</sup>:

$$\mu_{\text{FE}} = K \left( V_g - V_{\text{T,P}} \right)^\gamma, \quad (3)$$

where the exponent  $\gamma$  was correlated to the assumed carrier transport mode, and  $V_{\text{T,P}}$  to the threshold voltage or charge percolation threshold at a given temperature. Based on the less than a decade of gate-dependent  $\mu_{\text{FE}}$  modulation observed from amorphous  $\text{InZnO}/\text{InGaZnO}$  TFTs, they described the charge transport at low  $V_g$  as a trap-limited conduction (TLC) with the associated exponent of 0.7 and the high- $V_g$  transport as mediated by percolation transport with the related exponent of 0.1. Similar gate-dependent  $\mu_{\text{FE}}$  and exponents have been observed in the case of polycrystalline  $\text{ZnO}$  TFTs<sup>11,12</sup>.

Upon utilizing the power law relationship to empirically analyze the  $\mu_{\text{FE}}$  vs.  $V_g$  dependence, two different regimes are similarly identified in our gate-dependent mobility data obtained from the ultrathin  $\text{TiO}_x$  TFT, but, with very different exponent values as shown in Fig. 2c; at high  $V_g$  ( $>60 \text{ V}$ ), the exponent of 0.78 was obtained, indicating that the transport lies around the TLC according to the model proposed by Lee et al. However, at  $V_g < 60 \text{ V}$ , the obtained exponent is 2.18, far outside of the previously observed upper limit of 0.7<sup>16</sup>; in fact, such a high exponent value has never been reported for metal oxide TFT to our knowledge. As discussed, next, we attribute this to a high density of band-tail states that mediate the charge transport via VRH with the varying position of Fermi level ( $E_F$ ) prescribed by given  $V_g$  accessing different distributions of band-tail states capable of supporting the VRH.

**Origin of band-tail states.** First, in order to ascertain the stoichiometry of the  $\text{TiO}_x$  film and examine the presence of defects such as oxygen vacancies, high-resolution X-ray photoelectron spectroscopy (XPS) spectra were obtained from the prepared  $\text{TiO}_x$  film subjected to the post-ALD forming gas annealing (Fig. 3a, c) and compared with the data from a control  $\text{TiO}_x$  film after similar post-ALD annealing carried out in pure  $\text{O}_2$  (Fig. 3b, d). The defect states in metal oxides, typically originating from oxygen vacancies or interstitial hydrogen, are by nature shallow states generally existing very close to the conduction band edge. In the case of  $\text{TiO}_2$ , various reports have estimated that such shallow states exist at  $\sim 10$ – $260 \text{ meV}$  below the conduction band edge, among which those related with hydrogen interstitials are relatively closer to the conduction band edge than the oxygen vacancy states<sup>43–46</sup>. When the  $\text{TiO}_x$  ALD is carried out at lower

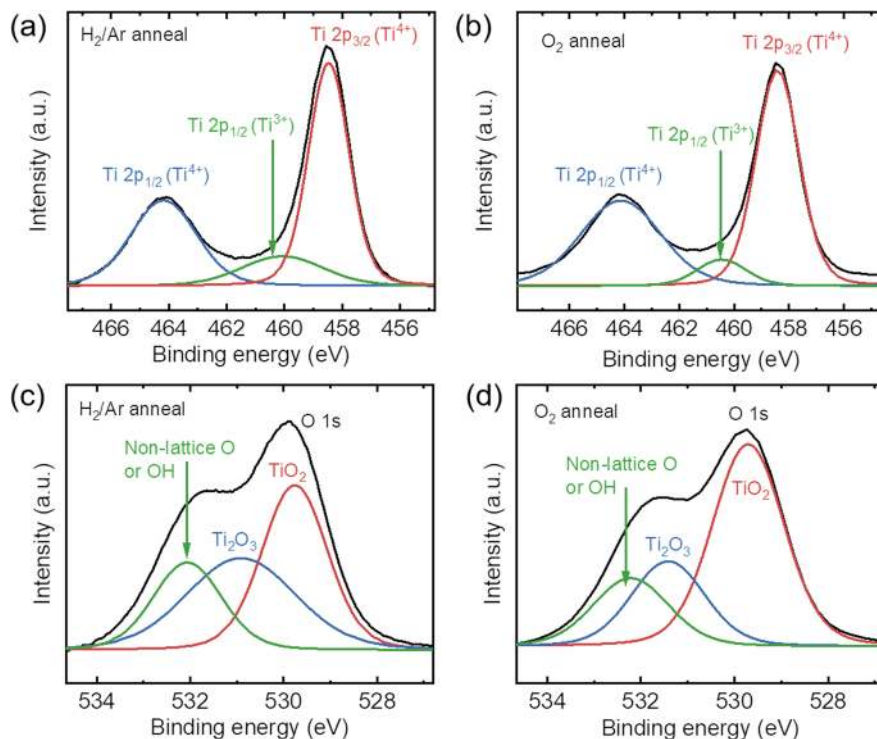


**Fig. 3 Processing-dependent stoichiometry and oxygen vacancies in ultrathin TiO<sub>x</sub>.** High-resolution XPS spectra of Ti 2p (top row) and O 1s (bottom row) of ultrathin TiO<sub>x</sub> film annealed in: **a, c** forming gas (4% H<sub>2</sub>/Ar); **b, d** TiO<sub>x</sub> film annealed in O<sub>2</sub>.

temperatures, such as 85 °C in our case, a high density of defect states is generally expected to exist within the deposited film.

As seen in the XPS spectra (Fig. 3a, b), both the Ti<sup>4+</sup> peaks, viz. Ti<sup>4+</sup> 2p<sub>3/2</sub> and Ti<sup>4+</sup> 2p<sub>1/2</sub>, correspond to TiO<sub>2</sub> lattice, whereas the Ti<sup>3+</sup> peak (Ti<sup>3+</sup>+2p<sub>1/2</sub>) is related to a reduced, Ti<sub>2</sub>O<sub>3</sub> lattice structure. The change in the peak intensities can be attributed to the difference in the electronic states of Ti in the two different samples. The sample annealed in forming gas (Fig. 3a) exhibited ~90 % larger area for Ti<sup>3+</sup> peaks and ~17 % area decrease for Ti<sup>4+</sup> peak, in comparison with oxygen-annealed sample (Fig. 3b). This observation indicates that the annealing in forming gas removes oxygen atoms from the TiO<sub>2</sub> lattice, reducing the concentration of Ti<sup>4+</sup>, resulting in the increase in Ti<sup>3+</sup> and the fraction of Ti<sub>2</sub>O<sub>3</sub><sup>47–49</sup>. The difference in the composition of the above samples was cross-confirmed by the peak shift and estimating the change in area of the O 1s XPS spectrum (Fig. 3c, d). The as-acquired O 1s peak was deconvoluted into three peaks with binding energies of 529.73, 531.22, and 532.23 eV, each corresponding to lattice oxygen (TiO<sub>2</sub>), reduced Ti<sub>2</sub>O<sub>3</sub>, and non-lattice oxygen (e.g., -OH, wherein hydrogen can originate from water used as an oxidant during ALD or forming gas annealing), respectively. In the forming-gas-annealed sample (Fig. 3c), the lattice oxygen peak (529.76 eV) exhibited a decrease in its area by ~28%, while the area of the Ti<sub>2</sub>O<sub>3</sub> peak (530.92 eV) and non-lattice oxygen peak (532.03 eV) increased by ~55% and ~12%, respectively, compared with the oxygen-annealed sample (Fig. 3d). These data, along with the Ti 2p XPS spectral analysis, thus confirm that the forming gas annealing led to the formation of oxygen vacancies in the lattice by the consumption of lattice oxygen to form a larger proportion of reduced Ti<sub>2</sub>O<sub>3</sub><sup>47</sup>.

To identify the effect of oxygen vacancies on the gate-dependent mobility, transfer characteristics were measured from a control TFT fabricated on the oxygen-annealed ultrathin TiO<sub>x</sub> film (Fig. 4a). Compared with the forming-gas-annealed TiO<sub>x</sub> TFT (Fig. 2b), the on-state drain current was decreased by 2 decades even at higher V<sub>d</sub> (=100 V), whereas the off-state current

was also increased by 2 decades, rendering the current modulation ratio significantly decreased down to only 2 decades. The observed increase in off-state currents is consistent to the notion that annealing the defective ultrathin TiO<sub>x</sub> film in oxygen environments reduces the concentration of oxygen vacancy (i.e., charge trap) and the number of trapped charge carriers within the TiO<sub>x</sub> film. Moreover, the oxygen-annealed device featured a markedly smaller difference between V<sub>th</sub> (~55.2 V) and V<sub>on</sub> (~46.4 V) compared with the forming-gas-annealed TiO<sub>x</sub> device (i.e., V<sub>th</sub> = ~48.5 V and V<sub>on</sub> = ~24.6 V), reaffirming the reduced charge trap density, given that the difference between V<sub>th</sub> and V<sub>on</sub> can be majorly attributed to the charge trap concentration within the channel of a TFT, since within the V<sub>on</sub> < V<sub>g</sub> < V<sub>th</sub> regime, most charge carriers are induced into trap states and/or tail states that exhibit low mobility<sup>36</sup>. Meanwhile, as we have postulated earlier, the primary charge transport in the on-state is likely mediated by the defect states associated with oxygen vacancies, and, thus, the decreased oxygen vacancy concentration should decrease the on-state current, as observed in the oxygen-annealed TiO<sub>x</sub> TFT (Fig. 4a). Likewise, the field-effect mobility was decreased by ~3 decades (Fig. 4b) with mobility modulation decreased to 4 decades compared with the forming-gas-annealed TiO<sub>x</sub> device (Fig. 2c) with ~6 decades of mobility modulation, strongly suggesting the role of defect states in the V<sub>g</sub>-induced mobility modulation.

Considering the ultrathin thickness of the TiO<sub>x</sub> film, it is also possible that the surface defects and associated states may have an impact on the TFT characteristics. In order to test this premise, we spin-coated 300 nm of poly(methyl methacrylate) (PMMA) on top of the TFT devices fabricated from the forming-gas-annealed ultrathin TiO<sub>x</sub> film. While the PMMA-topcoat is expected to only passivate the surface defects, the device characteristics of the PMMA-topcoat TiO<sub>x</sub> TFT (Fig. 4c) displayed only a marginal improvement in the transfer characteristics. For instance, both on- and off-state currents were only slightly increased, resulting in a minor increase in the maximum

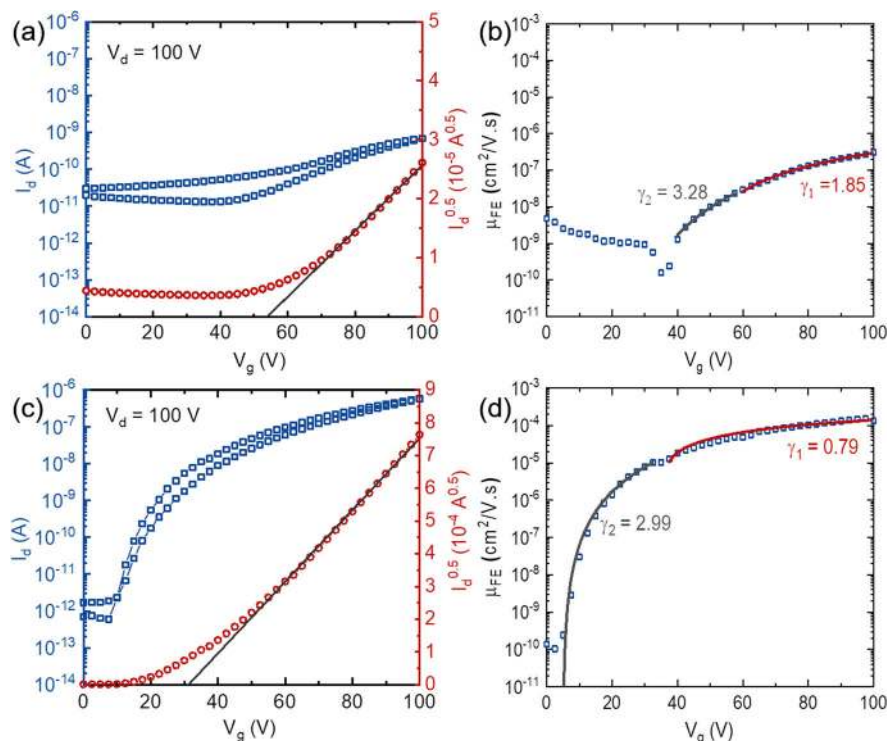


**Fig. 4 Role of oxygen vacancy defects in mediating VRH transport.** **a** Transfer characteristics of the TiO<sub>x</sub> TFT ( $W/L = 500 \mu\text{m}/5 \mu\text{m}$ ) fabricated using ultrathin TiO<sub>x</sub> film annealed in oxygen atmosphere (15 min at 400 °C followed by 15 min at 600 °C); **b**  $\mu_{FE}$  variation with  $V_g$  with power law fits for  $V_g > 50$  V and  $V_g < 50$  V. The exponent values of 1.85 and 3.28 indicate that the carrier transport occurs via VRH. The decrease in the number of available defects states however restricts the charge mobility. **c** Transfer characteristics of the TiO<sub>x</sub> TFT ( $W/L = 500 \mu\text{m}/5 \mu\text{m}$ ) fabricated using forming gas annealing and the PMMA top-coat, leading to the passivation of surface defects and, consequently, a small increase in the on-state current due to decreased carrier scattering. **d**  $\mu_{FE}$  variation with gate voltage and power law fit for  $V_g > 40$  V and  $V_g < 40$  V with the exponents of 0.79 and 2.99 indicating the VRH transport at low  $V_g$  changing toward TLC transport at high  $V_g$ .

saturation mobility. The device also featured  $\sim 6$  decades of current on–off ratio, largely identical to the value obtained without the PMMA surface passivation while  $V_{th}$  and  $V_{on}$  exhibited a slight decrease (by  $\sim 10$  V). As depicted in Fig. 4d, the field-effect mobility showed  $\sim 6$ -decade modulation with the power law exponents of 0.79 and 2.99, respectively, for high- $V_g$  and low- $V_g$  regimes, all nearly same as the values obtained from the TiO<sub>x</sub> device without the PMMA-topcoat, highlighting that the surface defect states have a minor influence on the observed, large gate-induced modulation of charge mobility, not interfering with the inherent charge carrier transport in the ultrathin TiO<sub>x</sub> thin film.

**Bi-exponential density of states.** Based on the correlations drawn between the transfer characteristics and XPS analysis discussed above, it can be established that the oxygen vacancies within the bulk of the TiO<sub>x</sub> film mediate the charge carrier transport in the ultrathin TiO<sub>x</sub> TFT. However, the meaning of the large power law exponent still remains unexplained, which to our knowledge has never been reported in the case of oxide semiconductors. During the postulation of Eq. (3) for TLC mode in oxide TFTs, Lee et al. have correlated the value of exponent to the characteristics of the band-tail density of states through  $2(T_0/T - 1)$ , where  $T_0$  is the characteristic temperature of band-tail states<sup>16</sup>. In fact, a similar empirical relationship has been discussed previously in other semiconductor systems such as organic TFTs<sup>50–52</sup>. Interestingly, Meijer et al. have analytically derived the identical mobility vs.  $V_g$  power law relationship based on the VRH transport of charge carriers through the band-tail states in

organic semiconductors<sup>50</sup>. They report the expression,

$$I_d = A(C_i(V_g - V_{on}))^{\left(\frac{2T_0}{T} - 1\right)}, \quad (4)$$

where  $T_0$  being the characteristic temperature of band-tail density of states, and  $A$  the proportionality constant dependent on  $T$  and other material parameters. Considering that  $\sigma_d = en\mu$ , where  $e$  is the elementary charge and  $n = \frac{C_i(V_g - V_{on})}{et_s}$  with  $t_s$  being the thickness of the charge accumulation layer, the Eq. (4) becomes expressing the identical power relation to Eq. (3) suggested by Lee et al. Despite the fact that both the models originate from slightly different analytical approaches, they arrive at the same power law relation between mobility and  $V_g$ , especially with the identical power law exponent. Lee’s model has presented the TLC transport in oxide semiconductors while Meijer et al. have formally referred the transport mode as VRH; the origin of both the transport mechanisms can be essentially attributed to localized band-tail states originating from the material being amorphous or highly defective. In TLC, the free electrons in the conduction band are responsible for the current flow with defect states acting as charge traps, whereas in the case of VRH, high density of trap states supports the hopping transport of charge carriers, thus effectively exhibiting the current flow. Our large exponent value suggests that VRH being the governing charge transport mechanism at low  $V_g$ . There are numerous past literatures studying VRH transport in organic TFT utilizing the same model and reporting similarly large exponents. The parameter  $T_0$  describes the width of exponential distribution of density of band-tail states<sup>53</sup>. In the case of our device, the value of exponent at low  $V_g$  (2.18 in Fig. 2c) corresponds to  $T_0 = 622.8$  K (i.e. 53.6 meV).

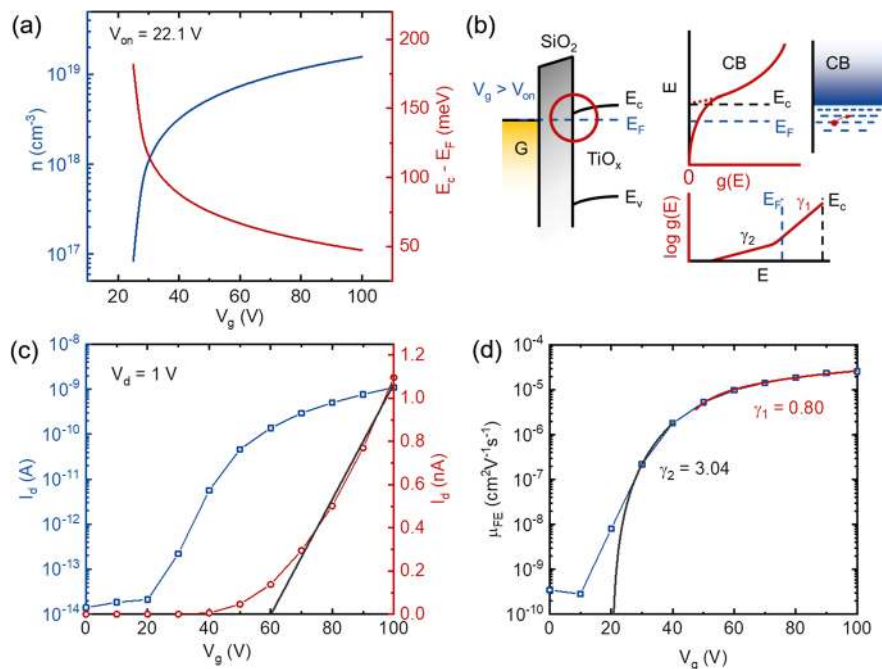


**Fig. 5 Bi-exponential density of states and VRH transport.** **a** Variation in  $n$  (blue line) and the position of  $E_F$  compared with  $E_C$  with respect to the  $V_g$  (red line) changed above  $V_{on}$ . **b** Schematic showing transistor band diagram across the gate-insulator-semiconductor stack (left); more details of the area marked by a red circle (top-middle) showing the electron energy ( $E$ ) vs. density of states ( $g$ ), where CB denotes the conduction band with characteristic parabolic  $g(E)$ ; bi-exponential variation of density of states ( $g(E)$ ) with energy near  $E_C$  (bottom-middle);  $E_F$  is inside the band-tail and moving closer to  $E_C$  when  $V_g > V_{on}$ , thus supporting the charge (red dot) conduction via hopping through the localized states (indicated by the red arrow) depicting VRH phenomena (right). **c** Linear-regime transfer characteristics extracted from the output characteristics of ultrathin  $\text{TiO}_x$  TFT prepared by forming-gas annealing. **d** Corresponding linear mobility variation with gate voltage with the power-law exponent for VRH regime at low  $V_g$  exhibiting the value of 3.04 and the TLC transport regime at high  $V_g$  exhibiting the value of 0.8.

This value is comparable to the values reported for VRH in organic TFTs (~450–550 K for poly(3-hexylthiophene) (P3HT) and poly(p-phenylene vinylene)) which, similar to our system, is predominantly amorphous<sup>54,55</sup>. This evidence supports that the VRH through localized band states is indeed mediating the charge transport in our system and suggests that it is also playing a role in exhibiting large mobility modulation.

Finally, it is possible to explain the observed two different power-law exponents in the  $V_g$ -dependent mobility data. Essentially, when  $V_g$  is varied in a given voltage range, the  $E_F$  in the transistor channel is sweeping through the density of band-tail states ( $g(E)$ ) having a bi-exponential distribution<sup>56</sup>.  $V_g$  causes the change in the carrier density,  $n$ , though  $n = \frac{C_i(V_g - V_{on})}{e t_{\tau}}$ , which in turn varies the  $E_F$  through  $E_C - E_F = k_b T \log(N_c/n)$ , with  $k_b$  being the Boltzmann constant and  $N_c$  the effective density of states of conduction band. These  $V_g$ -dependent  $n$  and  $E_F$  are illustrated in Fig. 5a. As  $V_g$  is increased,  $E_F$  is being moved closer to  $E_C$  (i.e., decreasing  $E_C - E_F$  from 180 meV to 50 meV). During the course of this sweep,  $E_F$  is probing the exponential distribution of localized band-tail states with two different  $k_b T_o$  regimes (Fig. 5b), which manifest themselves as the two linear regimes in the  $\log(g(E))$  vs.  $E$  plot with the corresponding  $g(E)$  expressed as:

$$g(E) = A \exp\left[-\frac{(E_C - E)}{k_b T_{o1}}\right] + B \exp\left[-\frac{(E_C - E)}{k_b T_{o2}}\right], \quad (5)$$

with  $A$  and  $B$  being proportional constants, and  $\frac{-1}{k_b T_{o1}}$  and  $\frac{-1}{k_b T_{o2}}$  indicating the two slopes in the schematic plot, respectively. In the mobility vs.  $V_g$  plots, a smaller  $\gamma_1$  (at high  $V_g$ ) gives a larger slope and a large  $\gamma_2$  (at low  $V_g$ ) a lower slope. Thus, our data shows that by sweeping  $V_g$ , we have surveyed  $g(E)$  and revealed

the bi-exponential distribution of band-tail density of states, supporting the notion of the VRH charge transport mediated by localized band-tail states. Using the exponent values estimated in Fig. 2c,  $\gamma_2 = 2.18$  and  $\gamma_1 = 0.78$ , the values for both the  $T_o$  parameters can be calculated as  $T_{o2} = 622.8$  K (53.6 meV) and  $T_{o1} = 298.4$  K (25.7 meV), respectively. It should also be noted that over the course of  $V_g$  sweep assessed in this study,  $E_F$  is tracing the sub-bandgap region within 180 meV to 50 meV, which is much larger than the thermal energy at room temperature (~25 meV). Thus, at low- $V_g$  when the  $E_F$  is residing in deeper trap states, the carriers do not have sufficient energy to get thermally released into the conduction band and VRH transport prevails. However, when  $E_F$  starts accessing the trap states much closer to 50 meV at high- $V_g$ , a stochastic thermal release of the charge carriers into the conduction band starts taking place and the transport evolves towards majorly TLC, which is also sometimes referred to as multiple trapping and thermal release (MTR) transport. Previously, exhibition of VRH at room temperature has been demonstrated in the case of amorphous organic semiconductors<sup>50,52</sup>. In the case of amorphous oxide semiconductors, however, the prevalence of TLC or VRH has been reported to depend on temperature, where TLC prevails at room temperature and on decreasing the temperature VRH dominates the carrier transport<sup>42</sup>.

Meanwhile, it is worth noting that the  $T_o$  values observed from the VRH model in organic TFTs have been estimated from the linear-regime mobility vs.  $V_g$  data<sup>55</sup>, not from the saturation regime as discussed so far. To test whether the  $V_g$ -dependent, linear-regime mobility in the ultrathin  $\text{TiO}_x$  TFT still follows the VRH charge transport, we utilized the output characteristics of the ultrathin  $\text{TiO}_x$  TFT (Fig. 2a), extracting the linear-regime transfer characteristics at  $V_d = 1$  V (Fig. 5c), which allows the evaluation of linear-regime  $\mu_{FE}$ .

The resulting  $\mu_{FE}$  vs.  $V_g$  plot in Fig. 5d clearly exhibits the two-exponent power law with 5-decade gate-dependent mobility modulation and the exponent values largely consistent with those observed in the saturation regime. This not only confirms the bi-exponential distribution of band-tail states but also further supports the correlation between the VRH transport and the large exponent at low  $V_g$  in the ultrathin  $TiO_x$  TFT regardless of the saturation or linear device operation regimes.

## Conclusions

In summary, the ultrathin amorphous  $TiO_x$  TFT fabricated by low-temperature ALD was investigated to explore the origin of large gate-dependent mobility modulation observed in ultrathin metal oxide TFTs. The large  $\sim 6$ -decade, gate-induced mobility modulation observed in the studied ultrathin  $TiO_x$  TFT could be associated with the presence of band-tail defects, such as bulk oxygen vacancies, based on the physicochemical analysis of  $TiO_x$  prepared under varying post-ALD thermal treatments and the accompanying TFT device characterization. By comparing the empirical power law relationship of the gate-dependent mobility in metal oxide TFTs with the analytic model previously derived for organic semiconductors, the large power-law exponent, which drives the large gate-induced mobility modulation, was identified to be originating from the VRH transport of charge carriers through the band-tail states of ultrathin  $TiO_x$ , with its bi-exponential density of states reflected on the two different power-law exponent regimes in the gate-dependent mobility. The results highlight rather unusual and counterintuitive roles of defect states within ultrathin metal oxides in possibly enabling some of the high performance parameters in associated TFT devices, as best exemplified by the increased off-state current accompanied by the reduced device on-off ratio upon the oxidative annealing of ultrathin  $TiO_x$  against the typical notion that such an oxidative annealing in metal oxide transistors would reduce the background carrier density while increasing the on-off ratio.

## Methods

**Fabrication of  $TiO_x$  TFT.** The  $TiO_x$  thin film was deposited using Cambridge Nanotech Savannah S100 ALD system (base pressure  $\sim 0.45$  Torr) at  $85^\circ\text{C}$  on oxygen-plasma-cleaned Si ( $p^{++}$ ) substrate with 300 nm dry thermal oxide. During each ALD cycle, titanium (IV) isopropoxide and water vapors were alternatively pulsed each for 0.4 s with 5-s interval under continuous  $N_2$  flow. In total, 75 cycles were used to deposit  $TiO_x$  film thickness of 3.5 nm (estimated by spectroscopic ellipsometry; J.A. Woollam M-2000FI). Unless otherwise stated, as deposited films were then annealed in forming gas (4%  $H_2/Ar$ ) using a rapid thermal processor (RTP; Modular Process Technology, RTP-600S) at  $400^\circ\text{C}$  for 15 min followed by  $600^\circ\text{C}$  for 15 min. The TFT devices were fabricated with electron-beam lithography using the bilayer resist scheme (PMGI SF6 underlayer and ZEP 5200 A imaging layer) followed by lift-off of the evaporated contact metal stack consisting of 30 nm Al, 30 nm Ti, and 40 nm Au (bottom to top), to pattern source-drain electrodes with channel length of  $5\ \mu\text{m}$  and width  $500\ \mu\text{m}$ . The schematic of the bottom gate top contact TFT device investigated in this study is shown in Fig. 1a.

**Material characterization.** The crystallinity of the  $TiO_x$  film was characterized by XRD (Rigaku Ultima III diffractometer), operating in the Bragg configuration using  $Cu\ K_\alpha$  radiation ( $1.54\ \text{\AA}$ ) with a scan range from  $10^\circ$  to  $80^\circ$  and a scan rate of  $0.38^\circ\ \text{min}^{-1}$  to acquire the XRD spectra. The chemical bonding characteristics of prepared samples were characterized by XPS using a custom-built XPS system equipped with a hemispherical electron energy analyzer (SPECS) and Al  $K_\alpha$  X-ray source (1.487 keV, SPECS). The sample crystallinity was also further examined by extremely surface-sensitive, LEED inside an ultra-high-vacuum (UHV) chamber (base pressure,  $2 \times 10^{-10}$  Torr) using a low energy electron microscope (LEEM) located at the Electron Spectro-Microscopy (ESM, 21-ID-2) beamline of the National Synchrotron Light Source II (NSLS-II). After being transferred to the UHV chamber, the samples were annealed at mild temperature of  $250^\circ\text{C}$  to remove adsorbed surface contaminants from air. All measurements were conducted at room temperature and using 30 eV incident electron energy.

## Data availability

All the relevant data acquired or analyzed in support of the findings reported in this study are available from Materials Cloud Archive (<https://doi.org/10.24435/materialscloud:1t-g7>) or the corresponding author upon request.

Received: 1 July 2020; Accepted: 3 November 2020;

Published online: 03 December 2020

## References

1. Thomas, S. R., Pattanasattayavong, P. & Anthopoulos, T. D. Solution-processable metal oxide semiconductors for thin-film transistor applications. *Chem. Soc. Rev.* **42**, 6910 (2013).
2. Yu, X., Marks, T. J. & Facchetti, A. Metal oxides for optoelectronic applications. *Nat. Mater.* **15**, 383–396 (2016).
3. Wager, J. F. TFT technology: advancements and opportunities for improvement. *Inf. Display* **36**, 9–13 (2020).
4. Sugii, N. Low-power-consumption fully depleted silicon-on-insulator technology. *Microelectron. Eng.* **132**, 226–235 (2015).
5. Kornblum, L. Conductive oxide interfaces for field effect devices. *Adv. Mater. Interfaces* **6**, 1–22 (2019).
6. Lee, H. J., Moon, T., An, C. H. & Hwang, C. S. 2D electron gas at the interface of atomic-layer-deposited  $Al_2O_3/TiO_2$  on  $SrTiO_3$  single crystal substrate. *Adv. Electron. Mater.* **5**, 1–7 (2019).
7. Seok, T. J. et al. Field-effect device using quasi-two-dimensional electron gas in mass-producible atomic-layer-deposited  $Al_2O_3/TiO_2$  ultrathin ( $<10\ \text{nm}$ ) film heterostructures. *ACS Nano* **12**, 10403–10409 (2018).
8. Li, S. et al. Nanometre-thin indium tin oxide for advanced high-performance electronics. *Nat. Mater.* **18**, 1091–1097 (2019).
9. Nagao, Y. et al. Experimental characterization of the electronic structure of anatase  $TiO_2$ : Thermopower modulation. *Appl. Phys. Lett.* **97**, 172112 (2010).
10. Jae-Woo, Park, Dongyun, Lee, Hakyoung, Kwon & Seunghyup, Yoo Improvement of on-off-current ratio in  $TiO_x$  Active-channel TFTs using  $N_2O$  plasma treatment. *IEEE Electron Device Lett.* **30**, 362–364 (2009).
11. Lin, Y.-H. et al. High-performance ZnO transistors processed via an aqueous carbon-free metal oxide precursor route at temperatures between  $80$ – $180^\circ\text{C}$ . *Adv. Mater.* **25**, 4340–4346 (2013).
12. Tiwale, N., Senanayak, S. P., Rubio-Lara, J., Alaverdyan, Y. & Welland, M. E. Optimization of transistor characteristics and charge transport in solution processed ZnO thin films grown from zinc neodecanoate. *Electron. Mater. Lett.* **15**, 702–711 (2019).
13. Kuan, C. I., Lin, H. C., Li, P. W. & Huang, T. Y. High-performance submicrometer ZnON thin-film transistors with record field-effect mobility. *IEEE Electron Device Lett.* **37**, 303–305 (2016).
14. Wei Shih, C., Chin, A., Fu Lu, C. & Fang Su, W. Remarkably high mobility ultra-thin-film metal-oxide transistor with strongly overlapped orbitals. *Sci. Rep.* **6**, 2–7 (2016).
15. Ju, S. et al. High performance ZnO nanowire field effect transistors with organic gate nanodielectrics: effects of metal contacts and ozone treatment. *Nanotechnology* **18**, 155201 (2007).
16. Lee, S. et al. Trap-limited and percolation conduction mechanisms in amorphous oxide semiconductor thin film transistors. *Appl. Phys. Lett.* **98**, 203508 (2011).
17. Zhu, L. et al. Ligand-free rutile and anatase  $TiO_2$  nanocrystals as electron extraction layers for high performance inverted polymer solar cells. *RSC Adv* **7**, 20084–20092 (2017).
18. Lu, H., Tian, W., Gu, B., Zhu, Y. & Li, L.  $TiO_2$  electron transport bilayer for highly efficient planar perovskite solar cell. *Small* **13**, 1–9 (2017).
19. Liu, M., Johnston, M. B. & Snaith, H. J. Efficient planar heterojunction perovskite solar cells by vapour deposition. *Nature* **501**, 395–398 (2013).
20. Zhang, Y. et al. Dopamine-crosslinked  $TiO_2$ /perovskite layer for efficient and photostable perovskite solar cells under full spectral continuous illumination. *Nano Energy* **56**, 733–740 (2019).
21. Liu, H. et al. Self-cleaning triboelectric nanogenerator based on  $TiO_2$  photocatalysis. *Nano Energy* **70**, 104499 (2020).
22. Meng, A., Zhang, L., Cheng, B. & Yu, J. Dual cocatalysts in  $TiO_2$  photocatalysis. *Adv. Mater.* **31**, 1–31 (2019).
23. Qian, R. et al. Charge carrier trapping, recombination and transfer during  $TiO_2$  photocatalysis: An overview. *Catal. Today* **335**, 78–90 (2019).
24. Wang, J., Yu, J., Zhu, X. & Kong, X. Z. Preparation of hollow  $TiO_2$  nanoparticles through  $TiO_2$  deposition on polystyrene latex particles and characterizations of their structure and photocatalytic activity. *Nanoscale Res. Lett.* **7**, 646 (2012).
25. Zhao, W. et al. Fabrication and characterization of high-performance thin-film transistors based on epitaxial Ta-doped  $TiO_2$  films. *IEEE Trans. Electron Devices* **66**, 4193–4197 (2019).

26. Katayama, M. et al. Field-effect transistor based on atomically flat rutile TiO<sub>2</sub>. *Appl. Phys. Lett.* **89**, 242103 (2006).
27. Zhang, J. et al. High performance anatase-TiO<sub>2</sub> thin film transistors with a two-step oxidized TiO<sub>2</sub> channel and plasma enhanced atomic layer-deposited ZrO<sub>2</sub> gate dielectric. *Appl. Phys. Express* **12**, 096502 (2019).
28. Sekizaki, S., Osada, M. & Nagashio, K. Molecularly-thin anatase field-effect transistors fabricated through the solid state transformation of titania nanosheets. *Nanoscale* **9**, 6471–6477 (2017).
29. Yajima, T., Oike, G., Nishimura, T. & Toriumi, A. Independent control of phases and defects in TiO<sub>2</sub> thin films for functional transistor channels. *Phys. Status Solidi* **213**, 2196–2202 (2016).
30. Ok, K.-C., Park, Y., Chung, K.-B. & Park, J.-S. The effect of Ta doping in polycrystalline TiO<sub>x</sub> and the associated thin film transistor properties. *Appl. Phys. Lett.* **103**, 213501 (2013).
31. Zhong, N., Cao, J. J., Shima, H. & Akinaga, H. Effect of annealing temperature on TiO<sub>2</sub>-based thin-film-transistor performance. *IEEE Electron Device Lett.* **33**, 1009–1011 (2012).
32. Shih, W. S., Young, S. J., Ji, L. W., Water, W. & Shiu, H. W. TiO<sub>2</sub>-based thin film transistors with amorphous and anatase channel layer. *J. Electrochem. Soc.* **158**, H609 (2011).
33. Wöbkenberg, P. H. et al. TiO<sub>2</sub> thin-film transistors fabricated by spray pyrolysis. *Appl. Phys. Lett.* **96**, 082116 (2010).
34. Park, J.-W., Lee, D., Kwon, H., Yoo, S. & Huh, J. Performance improvement of N-type TiO<sub>x</sub> active-channel TFTs grown by low-temperature plasma-enhanced ALD. *IEEE Electron Device Lett.* **30**, 739–741 (2009).
35. Zhong, N., Shima, H. & Akinaga, H. Mechanism of the performance improvement of TiO<sub>2-x</sub>-based field-effect transistor using SiO<sub>2</sub> as gate insulator. *AIP Adv.* **1**, 032167 (2011).
36. Hoffman, R. L. ZnO-channel thin-film transistors: channel mobility. *J. Appl. Phys.* **95**, 5813–5819 (2004).
37. Park, J.-W., Han, S.-W., Jeon, N., Jang, J. & Yoo, S. Improved electrical characteristics of amorphous oxide TFTs based on TiO<sub>x</sub> channel layer grown by low-temperature MOCVD. *IEEE Electron Device Lett.* **29**, 1319–1321 (2008).
38. Petti, L. et al. Metal oxide semiconductor thin-film transistors for flexible electronics. *Appl. Phys. Rev.* **3**, 021303 (2016).
39. Fortunato, E., Barquinha, P. & Martins, R. Oxide semiconductor thin-film transistors: a review of recent advances. *Adv. Mater.* **24**, 2945–2986 (2012).
40. Zhang, J. et al. Ultrathin-body TiO<sub>2</sub> thin film transistors with record on-current density, on/off current ratio, and subthreshold swing via O<sub>2</sub> annealing. *IEEE Electron Device Lett.* **40**, 1463–1466 (2019).
41. Bubel, S., Meyer, S., Kunze, F. & Chabinyk, M. L. Ionic liquid gating reveals trap-filled limit mobility in low temperature amorphous zinc oxide. *Appl. Phys. Lett.* **103**, 152102 (2013).
42. Lee, S. et al. Temperature dependent electron transport in amorphous oxide semiconductor thin film transistors. *2011 International Electron Devices Meeting* 14.6.1–14.6.4 (IEEE, 2011). <https://doi.org/10.1109/IEDM.2011.6131554>.
43. Panayotov, D. A. & Yates, J. T. n-Type doping of TiO<sub>2</sub> with atomic hydrogen-observation of the production of conduction band electrons by infrared spectroscopy. *Chem. Phys. Lett.* **436**, 204–208 (2007).
44. Yamakata, A., Ishibashi, T. & Onishi, H. Time-resolved infrared absorption spectroscopy of photogenerated electrons in platinized TiO<sub>2</sub> particles. *Chem. Phys. Lett.* **333**, 271–277 (2001).
45. Antila, L. J., Santomauro, F. G., Hammarström, L., Fernandes, D. L. A. & Sá, J. Hunting for the elusive shallow traps in TiO<sub>2</sub> anatase. *Chem. Commun.* **51**, 10914–10916 (2015).
46. Han, B. & Hang, Hu, Y. Investigation on H-containing shallow trap of hydrogenated TiO<sub>2</sub> with in situ Fourier transform infrared diffuse reflection spectroscopy. *Nanotechnology* **28**, 304001 (2017).
47. Bharti, B., Kumar, S., Lee, H.-N. & Kumar, R. Formation of oxygen vacancies and Ti<sup>3+</sup> state in TiO<sub>2</sub> thin film and enhanced optical properties by air plasma treatment. *Sci. Rep.* **6**, 32355 (2016).
48. Sanjinés, R. et al. Electronic structure of anatase TiO<sub>2</sub> oxide. *J. Appl. Phys.* **75**, 2945–2951 (1994).
49. Bertóti, I., Mohai, M., Sullivan, J. L. & Saied, S. O. Surface characterisation of plasma-nitrided titanium: an XPS study. *Appl. Surf. Sci.* **84**, 357–371 (1995).
50. Meijer, E. J. et al. Switch-on voltage in disordered organic field-effect transistors. *Appl. Phys. Lett.* **80**, 3838–3840 (2002).
51. Lustig, N., Kanicki, J., Wisnieff, R. & Griffith, J. Temperature dependent characteristics of hydrogenated amorphous silicon thin film transistors. *MRS Proc.* **118**, 267 (1988).
52. Horowitz, G., Hajlaoui, M. E. & Hajlaoui, R. Temperature and gate voltage dependence of hole mobility in polycrystalline oligothiophene thin film transistors. *J. Appl. Phys.* **87**, 4456–4463 (2000).
53. Vissenberg, M. C. J. M. & Matters, M. Theory of the field-effect mobility in amorphous organic transistors. *Phys. Rev. B* **57**, 12964–12967 (1998).
54. Tanase, C., Meijer, E. J., Blom, P. W. M. & de Leeuw, D. M. Unification of the hole transport in polymeric field-effect transistors and light-emitting diodes. *Phys. Rev. Lett.* **91**, 216601 (2003).
55. Tanase, C., Meijer, E. J., Blom, P. W. M. & de Leeuw, D. M. Local charge carrier mobility in disordered organic field-effect transistors. *Org. Electron.* **4**, 33–37 (2003).
56. Torricelli, F. Charge transport in organic transistors accounting for a wide distribution of carrier energies—part I: theory. *IEEE Trans. Electron Devices* **59**, 1514–1519 (2012).

### Acknowledgements

The research was carried out at the Center for Functional Nanomaterials (CFN) and National Synchrotron Light Source II (NSLS-II) of Brookhaven National Laboratory (BNL), which are supported by the U.S. Department of Energy, Office of Basic Energy Sciences, under Contract No. DE-SC0012704. C.-Y.N. and S.S. acknowledge the financial support by the U.S. Department of Energy, Office of Energy Efficiency & Renewable Energy, under Contract No. DE-EE0008423.

### Author contributions

N.T. and A.S. prepared TiO<sub>x</sub> samples. N.T. carried out device fabrication and electrical measurements. A.S. and S.S. carried out XPS measurements. A.S. conducted XRD measurements. Z.D. and J.T.S. performed LEED measurements. N.T. and C.-Y.N. planned experiments, analyzed data, assimilated and prepared initial draft. C.-Y.N. and J.T.S. conceptualized and supervised the study. All the authors discussed, commented on the draft and participated in finalizing the manuscript.

### Competing interests

The authors declare no competing interests.

### Additional information

Supplementary information is available for this paper at <https://doi.org/10.1038/s43246-020-00096-w>.

Correspondence and requests for materials should be addressed to C.-Y.N.

Peer review information Primary handling editor: Aldo Isidori.

Reprints and permission information is available at <http://www.nature.com/reprints>

Publisher's note Springer Nature remains neutral with regard to jurisdictional claims in published maps and institutional affiliations.



**Open Access** This article is licensed under a Creative Commons Attribution 4.0 International License, which permits use, sharing, adaptation, distribution and reproduction in any medium or format, as long as you give appropriate credit to the original author(s) and the source, provide a link to the Creative Commons license, and indicate if changes were made. The images or other third party material in this article are included in the article's Creative Commons license, unless indicated otherwise in a credit line to the material. If material is not included in the article's Creative Commons license and your intended use is not permitted by statutory regulation or exceeds the permitted use, you will need to obtain permission directly from the copyright holder. To view a copy of this license, visit <http://creativecommons.org/licenses/by/4.0/>.

This is a U.S. government work and not under copyright protection in the U.S.; foreign copyright protection may apply 2020